

# Exploration of strongly correlated states in $\text{SmB}_6$ through a comparison of its two-coil pick-up response to that of $\text{Bi}_2\text{Se}_3$

Sayantana Ghosh,<sup>1</sup> Sugata Paul,<sup>1</sup> Amit Jash<sup>1,2</sup>, Zachary Fisk,<sup>3</sup> and S. S. Banerjee<sup>1,\*</sup>

<sup>1</sup>Indian Institute of Technology Kanpur, Kanpur, Uttar Pradesh 208016, India

<sup>2</sup>Department of Condensed Matter Physics, Weizmann Institute of Science, 7610001 Rehovot, Israel

<sup>3</sup>Department of Physics and Astronomy, University of California at Irvine, Irvine, California 92697, USA



(Received 12 September 2022; revised 1 October 2023; accepted 3 October 2023; published 1 November 2023)

Authors of earlier studies on the Kondo insulator  $\text{SmB}_6$  revealed the presence of a bulk Kondo insulating gap between 30 and 50 K and the emergence of a conducting surface state only  $< 4$  K. Here, we compare the two-coil mutual inductance pick-up response of a  $\text{SmB}_6$  single crystal with that of a conventional topological insulator, a  $\text{Bi}_2\text{Se}_3$  single crystal. From these studies, we identify three distinct temperature regimes for  $\text{SmB}_6$ , viz., (i)  $T \geq T^*$  ( $\sim 66$  K), (ii) ( $\sim 40$  K)  $T_g \leq T < T^*$ , and (iii)  $T < T_g$ . At  $T^*$  in  $\text{SmB}_6$ , we observe a peak in the temperature-dependent AC pick-up signal which corresponds to the peak in the broad hump feature in the bulk DC susceptibility measurements and features in the resistivity measurements. A dip in the pick-up signal at  $T_g$  in  $\text{SmB}_6$  correlates with the evidence for the opening of a bulk Kondo gap in transport measurements. In this paper on our study of the pick-up signal in  $\text{SmB}_6$ , we suggest the presence of a thin (submicron-order thickness), high-conducting surface layer from a temperature just below  $T_g$ . In this  $T$  regime in  $\text{SmB}_6$ , the pick-up signal shows a distinct square root frequency ( $\nu$ ) dependence compared with the linear  $\nu$  dependence found in  $\text{Bi}_2\text{Se}_3$ . Across all the different  $T$  regimes, distinct AC frequency dependence and scaling properties are observed. Our results suggest that, above  $T^*$ , weak exchange interactions cause electrons to scatter from random ion sites. Electronic correlations gradually strengthen with the onset of Kondo-like hybridization, setting in from below  $T^*$ , and at  $T_g$ , a strongly correlated Kondo gap opens in the bulk of the material. The appearance of the thin, high-conducting surface layer is nearly coincident with the onset of the bulk Kondo insulating state below  $T_g$  in  $\text{SmB}_6$ .

DOI: [10.1103/PhysRevB.108.205101](https://doi.org/10.1103/PhysRevB.108.205101)

## I. INTRODUCTION

Samarium hexaboride ( $\text{SmB}_6$ ) belongs to the Kondo lattice insulator family where the itinerant  $d$  states of Sm ions hybridize with its localized  $f$  states to create a quenched lattice of screened  $f$ -electron moments. This leads to a correlated Kondo insulating state with a bulk Kondo gap [1–3], corresponding to a temperature scale  $T_g$ . Authors of most reports have suggested that  $T_g$  ranges between 30 and 50 K [4–6] in  $\text{SmB}_6$ . Resistivity  $\rho$  vs temperature ( $T$ ) [4–6] behavior in  $\text{SmB}_6$  shows a significant increase in  $\rho$  with lowering of temperature  $T < T_g$ . However, the rapid rise in  $\rho$  with decreasing  $T$  appears to saturate  $< 4$  K. This observation suggested the presence of a low-temperature conduction channel in  $\text{SmB}_6$ , which has triggered numerous debates [7]. Measurements have revealed that the saturation feature in  $\rho$  is independent of sample quality [4–6]. Unlike a typical band insulator,  $\text{SmB}_6$  possesses strongly interacting electronic states along with a significant spin-orbit interaction. Theoretical calculations have suggested that these spin-orbit interactions due to hybridization between the conduction band and  $f$  electrons result in gapless surface excitations with time-reversal symmetry [8,9]. Authors of such studies have implied that  $\text{SmB}_6$  belongs to a distinct category of strongly interaction-driven topological material [10–13]. However, the scenario

emerging from experiments is complex. Authors of transport studies [14–17] have seen a saturation of resistivity at low  $T$ . In these studies together with photoemission spectroscopy [18–21] and neutron scattering measurements [22], authors have suggested that the saturation in resistivity potentially could be related to a conducting surface state in  $\text{SmB}_6$  at low temperatures ( $< 4$  K). This coincides with an insulating gap in the sample bulk, as seen from point contact spectroscopy [23]. While some measurements [24] have suggested that, at low  $T$ , de Haas–van Alphen (dHvA) oscillations correspond to conduction from two-dimensional (2D) surface states, some other measurements, however, have claimed the oscillations originate from bulk [25,26]. The dHvA quantum oscillation measurements [24,26,27] and angle-resolved photoemission spectroscopy (ARPES) [20,28,29] have shown that the measured effective mass of electrons at low  $T$  is low, whereas STM measurements have suggested a high effective mass [30]. A common feature of these studies is that, in  $\text{SmB}_6$ , there is the opening of a Kondo gap in the bulk at  $T_g \sim 30$ –50 K, with evidence suggesting a conducting surface state appearing at a much lower  $T$  ( $< 4$  K). Thus,  $\text{SmB}_6$  is an exotic Kondo insulator (KI) with the prospect of having a topological surface state at significantly low  $T$  [7,31–35]. In this paper, using the sensitive two-coil mutual inductance technique for  $\text{SmB}_6$ , we explore the  $T$  regime around  $T_g$  and attempt to identify features of conductivity emerging in the background of a bulk Kondo gap below  $T_g$ .

Typically, while electrical transport studies are quite popular to study topological insulator (TI) materials

\*Corresponding author: [satyajit@iitk.ac.in](mailto:satyajit@iitk.ac.in)

[13,19,36–41], in these measurements, the parallel conduction channels present through the bulk and the surface are admixed, and their individual contributions to the net conductivity are difficult to discern. In the noncontact-type two-coil mutual inductance technique [42–47], it was shown that, in conventional TI material  $\text{Bi}_2\text{Se}_3$ , the bulk and topological surface states give rise to unique and distinct frequency ( $\nu$ ) and  $T$ -dependent features. There is a linear frequency dependence in a temperature regime where topological surface states contribute to the electrical conductivity while a quadratic  $\nu$  dependence is found in the temperature regime where the bulk conductivity dominates [42,43]. In this paper, using the above technique, we compare the behavior of single-crystal  $\text{SmB}_6$  with a well-known noninteracting TI material, viz., single-crystal  $\text{Bi}_2\text{Se}_3$  [48,49]. We measure the in-phase pick-up signal ( $V'$ ) for the two single crystals at different temperatures ( $T$ ) and excitation frequencies ( $\nu$ ).  $\text{Bi}_2\text{Se}_3$  at low  $\nu$ ,  $< 100$  K shows thermally activated bulk conductivity. For  $\text{SmB}_6$ , we find completely different temperature scales. We see that the  $T$  dependent pick-up signal  $V'(T)$ , based on the behavior, can be separated into three distinct regimes: (i)  $T \geq T^* \sim 66$  K, (ii) ( $\sim 40$  K)  $T_g \leq T < T^*$ , and (iii)  $T < T_g$ . Around  $T^*$  in  $\text{SmB}_6$ , we observe a peak in the temperature-dependent AC pick-up signal which corresponds to the peak in the broad hump feature from the bulk DC susceptibility measurements. Near  $T^*$ , we also see a nonlinear dependence of the  $V'$  signal on  $\nu$  and the excitation field amplitude as well. Such features are absent in the pick-up signal at  $T < T_g$  and  $T > T^*$ . Bulk electrical conductivity measurement in our  $\text{SmB}_6$  single crystal shows a featureless slow increase in resistivity (decrease in conductivity) in regime (i). However, in regime (ii), the rate of increase in resistivity becomes significant, and in regime (iii), i.e., below  $T_g$ , there is a rapid increase in resistivity due to the opening of a Kondo insulating gap in the bulk. A detailed comparison of the  $V'(T)$  response at low  $T$  in  $\text{SmB}_6$  and  $\text{Bi}_2\text{Se}_3$  suggests the presence of a thin, high-conducting surface layer just below  $T_g$  in  $\text{SmB}_6$  with an insulating bulk. In this regime for  $\text{SmB}_6$ , we find the frequency-dependent pick-up response  $V'(\nu) \propto \nu^{1/2}$  as compared with  $V'(\nu) \propto \nu$  found in the surface conducting regime of the TI material  $\text{Bi}_2\text{Se}_3$ . In the bulk-dominated conductivity regime, viz., well above  $T_g$  in  $\text{SmB}_6$  and  $> 70$  K in  $\text{Bi}_2\text{Se}_3$ , both materials exhibit identical  $\nu^2$  dependence of  $V'$ . The  $\nu^{1/2}$  dependence is probably a result of the presence of strong  $f$ - $f$  electron correlations modifying the features of the conducting surface layer in  $\text{SmB}_6$ . Results of our investigations indicate that, above  $T^*$ , weak exchange interactions cause electrons to scatter from random ion sites. Electronic correlations gradually strengthen below  $T^*$  as Kondo hybridization begins, and finally, a strongly correlated bulk gap appears at  $T_g$ . Our results suggest the appearance of the thin, high-conducting surface layer is nearly coincident with the onset of the bulk Kondo insulating state below  $T_g$  in  $\text{SmB}_6$ .

## II. EXPERIMENTAL TECHNIQUE

The  $\text{SmB}_6$  single crystal grown by the aluminum flux method [25,35] has dimensions of  $0.9 \times 0.75 \times 0.2$  mm (see Sec. I in the Supplemental Material [50] for x-ray diffraction details). Wavelength-dispersive x-ray spectroscopy (WDS)

gives the average Sm:B stoichiometry close to 1:6 (see Sec. I in the Supplemental Material [50] for details). The  $\text{Bi}_2\text{Se}_3$  single crystal prepared by slow cooling stoichiometric melts of high-purity bismuth (Bi) and selenium (Se) powders [40,41,51] has dimensions of  $3.9 \times 2.5 \times 0.069$  mm (see Sec. II in the Supplemental Material [50] for characterization of the  $\text{Bi}_2\text{Se}_3$  single crystal). Figure 1(a) shows a schematic of our noncontact-type two-coil mutual inductance measurement setup [42,43], where  $\text{SmB}_6$  is kept between the excitation and pick-up coil. The physical dimensions, number of turns, and inductance of the two coils are closely matched (see Sec. III in the Supplemental Material [50]). Alternating current ( $I$ ) at frequency  $\nu$  sent in the excitation coil creates a time-varying magnetic field. This AC excitation magnetic field is experienced by the sample placed between the two coils. The magnetic response generated by the sample, in turn, induces a voltage in the pick-up coil, which is measured using a Stanford SR830 DSP lock-in amplifier. We have used a Janis closed-cycle cryostat for low-temperature measurements. If  $I_0$  is the peak amplitude of the AC excitation current in the excitation coil, then the induced pick-up voltage amplitude is  $V(\nu) = I_0 M \nu$ , where  $M$  is the mutual inductance that contains the sample response. Note that  $M$  is proportional to the AC susceptibility ( $\chi_{ac}$ ) of the sample as  $V = M(\frac{dI_{ac}}{dt})$  and  $V = -\mu_0 N k \zeta \chi_{ac}(\frac{dI_{ac}}{dt})$ , where  $\mu_0$  is the permeability of free space,  $N$  is the number of turns of the pick-up coil,  $k$  is the geometric filling factor,  $\zeta$  is the cross-sectional area of the coil (both coils have the same  $\zeta$ ), and  $\chi_{ac} = \chi' + i\chi''$ . Additionally, we use a 1.5-mm-thick oxygen-free high-conductivity (OFHC) copper sheet (with an insulating coat) with a hole of diameter 0.75 mm placed on top of the excitation coil, and the sample is placed just above the hole to reduce the pick-up signal due to stray fields around the sample [42]. The stray alternating magnetic field present around the sample [see Fig. 1(a)] induces a significant signal in the pick-up coil which often dominates over the response from the sample. The OFHC-Cu sheet with a conductivity of  $\sim 6 \times 10^7$  S  $\text{m}^{-1}$  has a skin depth  $\delta$  of  $\sim 200$   $\mu\text{m}$  for a 1 kHz AC field. Because the thickness of our OFHC-Cu sheet is greater than  $\delta$ , most of the stray AC field present outside the sample is shielded out by the Cu sheet, except the AC magnetic field over the hole [42]. Thus, the Cu sheet significantly cuts off the stray field contribution to the signal. The hole concentrates the AC magnetic field directly onto the sample placed just over the hole [42], and thus, the pick-up signal is predominantly contributed by the sample. This has been confirmed by finite element analysis using COMSOL Multiphysics software simulations reported in our earlier work [42]. The stray AC fields, however, constitute a significant fraction of the background signal in the pick-up coil. Note that, for every measurement, we subtract the background signal from total response such that the pick-up signals contain mainly the sample response. The background signal is measured at different  $T$  and  $\nu$  by removing the sample and placing just the Cu sheet with a hole between the coils.

In this two-coil technique, the AC pick-up voltage  $V = V' + iV''$ ; however, in this paper, we focus on the behavior of the in-phase signal  $V'$ . It is also known that, for a conducting sample, the AC field from the excitation coil induces

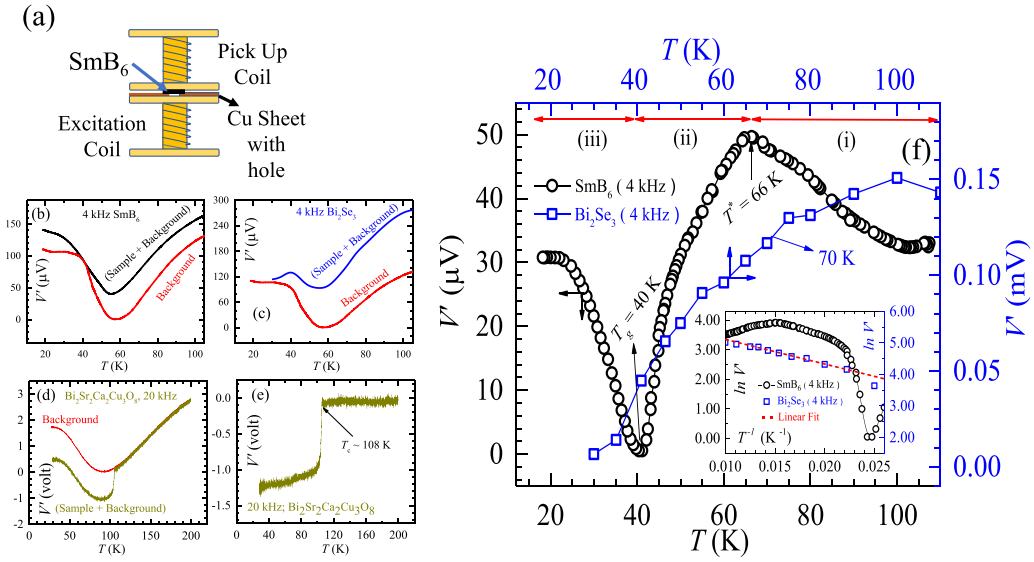


FIG. 1. Schematic of the setup and temperature dependence of the in-phase pick-up signal ( $V'$ ) of  $\text{SmB}_6$  and  $\text{Bi}_2\text{Se}_3$ . (a) Schematic of our two-coil setup with  $\text{SmB}_6$  placed between the coils. (b) Sample + background (black curve) and only background (red curve) of  $\text{SmB}_6$  for 4 kHz excitation frequency and 200 mA excitation current ( $I_0$ ). (c) Sample + background (blue curve) and only background (red curve) of  $\text{Bi}_2\text{Se}_3$  for 4 kHz excitation frequency and 200 mA excitation current ( $I_0$ ). (d) Sample + background (dark green curve) and only background (red curve) of BSCCO for 20 kHz excitation frequency and 200 mA excitation current ( $I_0$ ). (e)  $V'$  vs  $T$  data of BSCCO for 20 kHz excitation frequency and 200 mA excitation current ( $I_0$ ). (f)  $V'$  vs  $T$  data for  $\text{SmB}_6$  (black open circles) and  $\text{Bi}_2\text{Se}_3$  (blue open squares) both for 4 kHz excitation frequency and 200 mA excitation current ( $I_0$ ). Note that the left (black colored) and bottom (black colored) axes correspond to  $V'(T)$  data for  $\text{SmB}_6$  only and the right (blue colored) and top (blue colored) axes correspond to that for  $\text{Bi}_2\text{Se}_3$ . The three distinct temperature regimes (i)–(iii) for  $\text{SmB}_6$  are marked by red arrows. Inset shows the  $\ln V'$  vs  $T^{-1}$  plot for both  $\text{SmB}_6$  (black open circles) and  $\text{Bi}_2\text{Se}_3$  (blue open squares). Here, the left and right vertical axes correspond to  $\text{SmB}_6$  and  $\text{Bi}_2\text{Se}_3$ , respectively (with a common  $x$  axis). The linear fit (red dashed line) shows the activated nature of the conductivity of  $\text{Bi}_2\text{Se}_3$ , whereas a completely different nature is observed for  $\text{SmB}_6$ .

currents in the sample whose strength is proportional to the  $\nu$ -dependent electrical conductivity  $\sigma$  of the material. These currents in the sample induce a signal in the pick-up coil. As shown through Eq. (1) in Ref. [42], the pick-up signal is related to  $\sigma(\nu)$  of the material. Therefore, the pick-up signal in the two-coil technique not only depends on  $\chi$  but also on  $\sigma$ . While  $\text{Bi}_2\text{Se}_3$  is nonmagnetic, there is a discernible  $\chi$  response for  $\text{SmB}_6$ . Using the SQUID magnetometer, we measure  $\chi(T)$  for  $\text{SmB}_6$  over the  $T$  regime of interest. Normalizing the  $V'(T)$  response with  $\chi(T)$ , we obtain a signal which is representative of the behavior of  $\sigma(T)$  of the sample (details discussed subsequently). Another benefit of measuring the conductivity of the sample using the two-coil technique is that, depending on  $\nu$  of the excitation AC field, signals acquired closer to the conducting sample surface can be distinguished from those obtained from deeper within the sample volume. A low- $\nu$  AC excitation field penetrates deeper into a conducting sample (since  $\delta \propto \frac{1}{\sqrt{\nu\sigma}}$ ), which leads to a pick-up signal from a larger sample volume (which we will subsequently refer to as the bulk sample response) compared with a higher  $\nu$  AC field, which penetrates only into a thin layer (submicron-order thickness) close to the sample surface [see the estimate of skin depth ( $\delta$ ) for  $\text{Bi}_2\text{Se}_3$  in Sec. V of Ref. [42] and for  $\text{SmB}_6$  discussed later here]. This feature was previously used to distinguish between the behavior of bulk ( $\sigma_b$ ) and surface ( $\sigma_s$ ) electrical conductivity in a noninteracting TI,  $\text{Bi}_2\text{Se}_3$  single crystal [42,43,52]. We use the above

technique now to compare the  $V'$  behavior of single crystals of  $\text{SmB}_6$  and  $\text{Bi}_2\text{Se}_3$ .

### III. RESULTS

#### A. Comparison of $\text{SmB}_6$ and $\text{Bi}_2\text{Se}_3$ $V'(T)$ response

Figures 1(b) and 1(c) show  $V'(T)$  of the sample with background and only the background signal for  $\text{SmB}_6$  and  $\text{Bi}_2\text{Se}_3$ , respectively. For all these measurements, 200 mA excitation current and 4 kHz excitation frequency were used. Figure 1(d) shows the  $V'(T)$  behavior of a high-temperature superconductor  $\text{Bi}_2\text{Sr}_2\text{Ca}_2\text{Cu}_3\text{O}_8$  (BSCCO-2223; sample + background and the background for 200 mA excitation current and 20 kHz excitation frequency). The background signal of the Cu sheet with hole is the combined result of the AC field shielding contributions, from the solid regions of the copper sheet away from the hole and that from the regions around the hole. In Fig. 1(e), the background-subtracted  $V'(T)$  shows the expected increase in diamagnetic susceptibility below the superconducting transition temperature  $T_C \sim 108$  K of BSCCO-2223, which compares well with earlier two-coil measurements [43]. Figure 1(f) shows the background-subtracted  $V'(T)$  for  $\text{SmB}_6$  and  $\text{Bi}_2\text{Se}_3$  single crystals. For  $\text{Bi}_2\text{Se}_3$  (blue symbols),  $V'(T)$  decreases  $< 100$  K. The inset of Fig. 1(f) depicts a linear (see red dashed line)  $\ln V'(T)$  vs  $T^{-1}$  behavior, which is a feature of activated charge conductivity in bulk of  $\text{Bi}_2\text{Se}_3$ . At 4 kHz,  $\sigma_b$

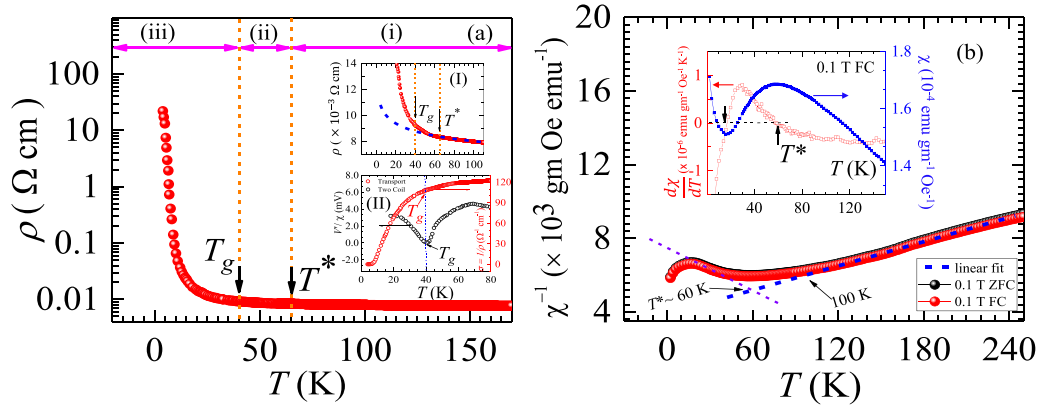


FIG. 2. Transport and DC susceptibility of  $\text{SmB}_6$  single crystal. (a) Four-probe based electrical resistivity ( $\rho$ ) vs  $T$  data for  $\text{SmB}_6$  single crystal. The figure identifies the three regimes (i)–(iii) marked by magenta arrows and two temperatures  $T_g$  and  $T^*$ . Inset (I) shows the behavior (blue dashed line) of the Hamann function  $\rho(T) \propto [1 - \frac{\ln(T/T_K)}{\sqrt{\ln^2(T/T_K) + s(s+1)\pi^2}}]$ , which fits the high- $T$  regime ( $T > T^*$ ) of the data. One sees the clear departure of  $\rho(T)$  from the Hamann fit from below  $\sim T^*$  (see discussion section of main text for additional details). Inset (II) shows  $V'(T)/\chi(T)$  response at 4 kHz excitation frequency (black circles) and bulk DC conductivity ( $\sigma$ ) response (red circles) of  $\text{SmB}_6$  from two-coil and transport experiments, respectively.  $\sigma$  starts to decrease at  $T_g = 40$  K, whereas  $V'(T)/\chi(T)$  shows significant increase from  $T_g = 40$  K. (b) DC magnetic susceptibility measurements on  $\text{SmB}_6$  show  $\chi^{-1}$  vs  $T$  plot for both zero-field-cooled (ZFC; red spheres) and field-cooled (FC; black spheres) under 0.1 T magnetic field. Blue dashed line shows the Curie Weiss fit  $> 100$  K. Linear back extrapolation (violet dashed line) marks the  $T^* \sim 60$  K. Inset shows  $\frac{d\chi}{dT}$  vs  $T$  (red open squares and left y axis) and  $\chi$  vs  $T$  (blue closed squares and right y axis) for 0.1 T FC.  $T^*$  is denoted by black arrows in both the main panel and the inset.

in  $\text{Bi}_2\text{Se}_3$  has the form  $V'(T) \propto \sigma_b(T) \propto \exp(-\frac{\Delta}{k_B T})$ , where  $\Delta$  is the activation energy scale. The activated behavior of bulk conductivity in  $\text{Bi}_2\text{Se}_3$  is produced due to the doped charges created by Se vacancies in the crystal [53]. We estimate the activation energy scale  $\Delta$  is  $\sim 5.92 \pm 0.31$  meV from the slope of the red dashed line in the inset of Fig. 1(f), which is consistent with previous results [42]. The behavior of  $V'(T)$  for the  $\text{SmB}_6$  crystal is completely different from that for  $\text{Bi}_2\text{Se}_3$ . In Fig. 1(f), we find that, with reducing  $T$  from 100 K,  $V'(T)$  of  $\text{SmB}_6$  initially increases and exhibits a peak at  $T^* \sim 66$  K. Below  $T^*$ ,  $V'(T)$  rapidly decreases to reach a minima at  $T_g \sim 40$  K [see Fig. 1(f)]. Below  $T_g$ ,  $V'(T)$  increases once again to finally saturate at low  $T$  for  $\text{SmB}_6$ .

### B. Transport and DC magnetization measurements of $\text{SmB}_6$

Figure 2(a) shows our standard four-probe measurements of resistivity  $\rho$  vs  $T$  for the  $\text{SmB}_6$  single crystal. We observe a monotonic increase in  $\rho$  with decreasing  $T$ . Approximately,  $\rho(T)$  shows a weak  $T$ -dependent regime from high  $T$  down to  $\sim 65$  K. Below 65 K,  $\rho(T)$  increases significantly and shows an exponential rise from  $T_g \sim 40$  K. This sharp increase in  $\rho$  at  $T < T_g$  results from the strongly correlated Kondo insulating gap opening in the bulk. This behavior of  $\rho(T)$  is consistent with earlier studies in  $\text{SmB}_6$  [4,5,14,15,54,55], and the value of  $T_g$  is also in a similar range [1,15,30]. Inset (I) of Fig. 2(a) shows that  $\rho(T)$  obeys the conventional Hamann fit [56] down to  $T^* \sim 65$  K and then starts to deviate from it. This has been elaborated upon in the discussion section later. Note that the minima in  $V'(T)$  of  $\text{SmB}_6$  [see Fig. 1(f)] occurs at the Kondo gap temperature  $T_g$ . Inset II of Fig. 2(a) shows the comparison of the effective conductivity derived from normalized pick-up response  $V'(T)/\chi(T)$  and the bulk conductivity [ $\sigma(T)$ ] response from transport (see the comparison up to 300 K in Sec. IV in the Supplemental Material [50]).

We observe that, from 80 to 40 K ( $= T_g$ ), while the electrical conductivity ( $\sigma$ ) changes by a small amount,  $V'(T)/\chi(T)$  drops significantly. At  $T < T_g$ , while the bulk  $\sigma$  drops rapidly due to formation of the Kondo gapped state,  $V'(T)/\chi(T)$  shows a significant increase. Note that the size of the cusplike feature at  $T^*$  is significantly diminished compared with the rise in  $V'(T)/\chi(T)$  seen below  $T_g$ . This difference suggests the enhancement in effective conductivity is from the thin surface layer below  $T_g$  in  $\text{SmB}_6$ . Although the feature in  $V'(T)$  at  $T^*$  [in Fig. 1(f)] is not prominent in  $V'(T)/\chi(T)$  [Fig. 2(a) inset II], it appears as a modulation in  $\rho(T)$  behavior, which is seen more clearly from the behavior of the absolute value of  $\frac{d\rho}{dT}$  vs  $T$  (log-log scale) around  $T^* = 65 \pm 2$  K (see Sec. V in the Supplemental Material [50]). A similar change is also seen here near  $T_g = 40 \pm 2$  K (see Sec. V in the Supplemental Material [50]).

The 0.1 Tesla isofield DC  $\chi(T)$  measurement (cryofree Cryogenics UK, SQUID magnetometer) for  $\text{SmB}_6$  single crystal is shown in the inset of Fig. 2(b) (blue data points). Below 300 K, there is a monotonic increase in  $\chi(T)$  as  $T$  is reduced, and it has a broad dome-shaped characteristic  $< 100$  K. We show that  $\chi(T)$  behavior for 0.1 Tesla zero-field-cooled (ZFC) and field-cooled (FC) conditions are identical, suggesting the absence of any irreversible magnetic component in  $\text{SmB}_6$  (see Sec. VI in the Supplemental Material [50]). Below 15 K, an increase in  $\chi(T)$  is observed. A similar nature of  $\chi(T)$  as in the inset of Fig. 2(b) was also seen earlier [35]. The broad dome feature in  $\chi(T)$  is usually considered to be related to the opening of a Kondo gap in the bulk of  $\text{SmB}_6$  [35,57]. However, the increase of  $\chi(T) < 15$  K has been suggested to be related to some fluctuating moments in the bulk of  $\text{SmB}_6$  [57] or the presence of paramagnetic impurities [58]. Note our  $T$  regime of interest in this paper is  $> 15$  K. From the  $\frac{d\chi}{dT}$  vs  $T$  plot in the inset of Fig. 2(b) (red data points), we see extrema ( $\frac{d\chi}{dT} = 0$ ) at  $T^* \sim 60 \pm 1$  K

TABLE I.  $T^*$  and  $T_g$  values determined from different techniques.

Technique	$T^*$ (K)	$T_g$ (K)
Two-coil	$66 \pm 1$	$40 \pm 1$
Resistivity	$65 \pm 2$	$40 \pm 1$
DC susceptibility	$60 \pm 1$	—

and at 15.5 K (shown by black arrows). The decrease in  $\chi(T)$  below  $T^*$  [Fig. 2(b) inset] coincides with a decrease in the pick-up signal  $V'(T)$  at 4 kHz below  $T^*$  [Fig. 1(f)]. This indicates the Kondo screening process starting in the bulk of  $\text{SmB}_6$  from below  $T^*$ . We do not see any distinguishing feature related to  $T_g$  either in  $\chi(T)$  or in  $\frac{d\chi}{dT}$ . Table I shows that  $T^*$  and  $T_g$  obtained from the two-coil measurements [Fig. 1(f)], transport [ $\rho(T)$  in Fig. 2(a)], and DC susceptibility [ $\chi(T)$  in Fig. 2(b) inset] measurements are all in a similar range to variations of 3–5 K. The variations are attributed to differences in cryogenic conditions in the three different setups used for our measurements. The inverse susceptibility  $\chi^{-1}$  vs  $T$  behavior for both 0.1 T ZFC and FC conditions are plotted in the main panel in Fig. 2(b). We see that, while at high  $T$  ( $> 100$  K), the data fit (blue dashed line) the Curie-Weiss law, i.e.,  $\chi(T) = \frac{C}{T-\theta}$ , with  $\theta = -230.2$  K and Curie constant  $C = 0.039 \text{ emu K g}^{-1} \text{ Oe}^{-1}$ , the data deviate significantly at low  $T < 100$  K. Similar features in  $\chi(T)$  of  $\text{SmB}_6$  have also been reported by other groups [55]. Note that, in other systems, such Curie-Weiss-like behavior is observed in strongly correlated itinerant electron scenarios without any long-range magnetic ordering [55,59–61]. Furthermore, Fig. 2(b) shows that, with lowering of  $T$ , there is a strong deviation from the

Curie-Weiss nature. A linear back extrapolation (dashed violet line) from low  $T$ , where  $\chi^{-1}$  has deviated significantly from the Curie-Weiss law, intersects with the back extrapolated Curie-Weiss fit from the high- $T$  regime. The intersection gives us a temperature scale  $\sim 60$  K, below which it appears that the correlations set in the system. Note that this  $T \sim 60$  K is close to our  $T^*$  value identified earlier. The above Curie-Weiss-like nature at high  $T$  and deviation from it at low  $T$  suggests the transition from an uncorrelated paramagnetic response regime to a strong electronic-correlation-dominated regime in  $\text{SmB}_6 < 60$  K.

### C. Comparison of surface conductivity of $\text{Bi}_2\text{Se}_3$ and $\text{SmB}_6$

At  $\nu = 4$  kHz, for  $\text{SmB}_6$ ,  $V'(T)$  in Fig. 1(f) increases for  $T < T_g$ . The minimum at  $T_g$  in  $\text{SmB}_6$  is like the  $V'(T)$  behavior in nonmagnetic  $\text{Bi}_2\text{Se}_3$ , albeit in  $\text{Bi}_2\text{Se}_3$ , this minimum was seen in  $V'(T)$  data taken at  $\nu = 65$  kHz [42]. In Fig. 3(a), we compare the  $V'(T)/\chi(T)$  data for  $\text{SmB}_6$  at 4 kHz with  $V'(T)$  data for the  $\text{Bi}_2\text{Se}_3$  single crystal measured at  $\nu = 65$  kHz. Recall that  $\text{Bi}_2\text{Se}_3$  has no inherent magnetism; therefore, the  $V'(T)$  behavior is due to its electrical conductivity  $\sigma(T)$  response, whereas in  $\text{SmB}_6$ ,  $V'(T)/\chi(T)$  gives the effective electrical conductivity behavior. In  $\text{Bi}_2\text{Se}_3$ ,  $\sigma(T) = \sigma_b(0) \exp(-\frac{\Delta}{k_B T}) + \frac{\sigma_s(0)}{C+DT}$ , where  $\sigma_b(0)$  and  $\sigma_s(0)$  are the temperature-independent bulk and topological surface state conductivities, respectively,  $D$  is related to electron-lattice scattering, and  $C$  is related to electron-electron ( $e-e$ ) interaction strength [38,42]. Due to the small value of the skin depth at high  $\nu = 65$  kHz, only a thin layer around the sample surface in the  $\text{Bi}_2\text{Se}_3$  is probed by the excitation field. Hence, in Fig. 3(a), at 65 kHz,  $< 70$  K, the contribution from the

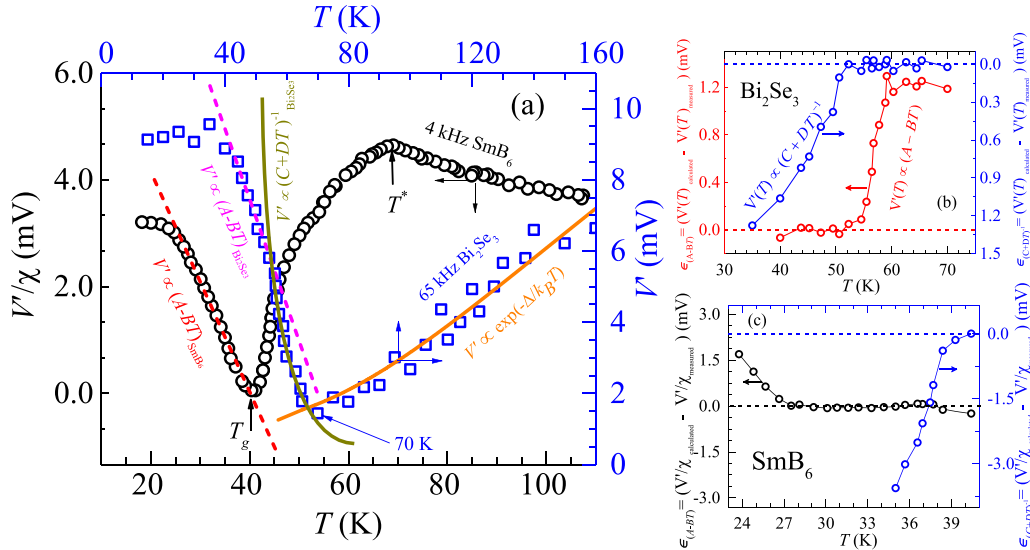


FIG. 3. Comparison of  $V'(T)$  of  $\text{Bi}_2\text{Se}_3$  and  $\text{SmB}_6$ . (a)  $V'(T)$  response of  $\text{Bi}_2\text{Se}_3$  and  $V'(T)/\chi(T)$  of  $\text{SmB}_6$  are denoted by blue open squares and black open circles, respectively. Note that the left (black colored) and bottom (black colored) axes correspond to  $V'(T)/\chi(T)$  data for  $\text{SmB}_6$  only and the right (blue colored) and top (blue colored) axes correspond to  $V'(T)$  data for  $\text{Bi}_2\text{Se}_3$ . Dark yellow fit shows  $V'(T) \propto 1/(C + DT)$  behavior of  $\text{Bi}_2\text{Se}_3$  surface state conductivity. Orange solid line fit shows  $V'(T) \propto \exp(-\frac{\Delta}{k_B T})$  behavior of  $\text{Bi}_2\text{Se}_3$  bulk state conductivity. Red and magenta dashed lines show distinct  $V'(T)/\chi(T) \propto (A-BT)$  and  $V'(T) \propto (A-BT)$  behavior of  $\text{SmB}_6$  and  $\text{Bi}_2\text{Se}_3$  surface conductivity, respectively. (b) Difference between  $V'(T)$  data calculated from the fits [ $\frac{1}{C+DT}$  and  $(A-BT)$ ] and from experiment for  $\text{Bi}_2\text{Se}_3$ , and (c) shows the difference between  $V'(T)/\chi(T)$  data calculated from the fits [ $\frac{1}{C+DT}$  and  $(A-BT)$ ] and from experiment for  $\text{SmB}_6$ .

TABLE II. Comparison of  $C$ ,  $D$  and  $A$ ,  $B$  values between  $\text{Bi}_2\text{Se}_3$  and  $\text{SmB}_6$ .

Sample	$C$	$D$	$A$	$B$
$\text{Bi}_2\text{Se}_3$ (65 kHz)	0.0052 mV <sup>-1</sup>	1.86 mV <sup>-1</sup> K <sup>-1</sup>	20.408 mV	0.249 mV K <sup>-1</sup>
$\text{SmB}_6$ (4 kHz)	0.0003 mV <sup>-1</sup>	0.79 mV <sup>-1</sup> K <sup>-1</sup>	8.49 mV	0.21 mV K <sup>-1</sup>

$\exp(-\frac{\Delta}{k_B T})$  dependence of bulk conductivity falls below the contribution from the  $T$ -dependent topological surface state conductivity of  $\text{Bi}_2\text{Se}_3$ . This results in the upturn feature in  $V'(T)$ , which serves as a signature of the contribution from TI surface conducting states. Figure 3(a) shows that, in the  $T$  range 50–70 K,  $V'(T)$  of  $\text{Bi}_2\text{Se}_3$  fits with the  $\frac{1}{C+DT}$  behavior as  $V'(T) \propto \sigma_s \propto \frac{1}{C+DT}$ . Note that a similar  $V'(T) \propto \frac{1}{C+DT}$  dependence has been reported in other crystals of  $\text{Bi}_2\text{Se}_3$  via pick-up coil measurements [42] and transport measurements [38]. From Fig. 3(a), we see that,  $< 50$  K, the behavior of  $V'(T)$  for  $\text{Bi}_2\text{Se}_3$  fits to a form  $[A-BT]$  (see magenta dashed line). In Fig. 3(b), we plot the value of the fit error at different  $T$ ,  $\epsilon_{(C+DT)^{-1}}(T) = [V'(T) \text{ calculated using } \frac{1}{C+DT}] - [V'(T) \text{ as measured}]$  and  $\epsilon_{(A-BT)}(T) = [V'(T) \text{ calculated with } A-BT] - [V'(T) \text{ as measured}]$  for  $\text{Bi}_2\text{Se}_3$ . It shows that  $\epsilon_{(C+DT)^{-1}} \approx 0$  between 70 and 50 K, while  $< 50$  K,  $\epsilon_{(A-BT)} \approx 0$ . This suggests  $(C+DT)^{-1}$  is a good fit to  $V'(T)$  data from 70 to 50 K, while  $< 50$  K,  $[A-BT]$  is a better fit to the data of  $\text{Bi}_2\text{Se}_3$ . Note that, in  $\text{SmB}_6$  for  $T < T_g$ , the upturn in  $V'(T)/\chi(T)$  follows a  $(A-BT)$  behavior [Fig. 3(a)]. The upturn cannot be ascribed to any bulk conductivity ( $\sigma$ ) features since the inset (II) of Fig. 2(a) has already shown the rapid decrease in  $\sigma$  due to Kondo localization below  $T_g$ . Furthermore, the inset of Fig. 2(b) also indicates that, below  $T^*$  (and below  $T_g \sim 40$  K), DC  $\chi(T)$  decreases. The upturn in  $V'(T) < 70$  K in  $\text{Bi}_2\text{Se}_3$  at high  $\nu = 65$  kHz had suggested the presence of high-conducting surface state features. Observation of a similar upturn in  $V'(T)/\chi(T)$ , below  $T_g$  in  $\text{SmB}_6$ , suggests the presence of a thin, high-conducting surface layer in this  $T$  regime. Figure 3(c) shows the fit error at different  $T$  for  $\text{SmB}_6$  using the same fit formula of  $[A-BT]$  and  $(C+DT)^{-1}$ , where  $V'(T)$  has been replaced by  $V'(T)/\chi(T)$  in the expression of  $\epsilon(T)$ . For  $\text{SmB}_6$ ,  $\epsilon_{(C+DT)^{-1}} \approx 0$  over  $\sim 2$  K below  $T_g = 40$  K. Below 38 K,  $\epsilon_{(C+DT)^{-1}}$  deviates significantly from 0, and in this regime,  $\epsilon_{(A-BT)} \approx 0$ . It has been suggested [42,62,63] that enhanced influence of  $e-e$  interaction effects at low  $T$  is a plausible source for the observed changes in  $T$  dependence of  $V'$  leading to even a low- $T$  ( $< 40$  K in  $\text{Bi}_2\text{Se}_3$  and  $< 27$  K in  $\text{SmB}_6$ ) saturation of  $V'(T)$ , as observed in Fig. 3(a). From the comparison of surface conductivity, we see that, while the  $T$  dependence of  $V'$  in  $\text{Bi}_2\text{Se}_3$  first shows  $\frac{1}{C+DT}$  behavior at the upturn below  $\sim 70$  K followed by  $[A-BT]$  behavior only  $< 50$  K, in  $\text{SmB}_6$ ,  $V'(T)$  shows  $[A-BT]$  behavior over a much wider  $T$  window which begins from just below  $T_g$ . Table II summarizes the  $C$ ,  $D$ ,  $A$ , and  $B$  values for  $\text{SmB}_6$  and  $\text{Bi}_2\text{Se}_3$ .

We estimate the typical thickness of the thin, high-conducting surface layer seen below  $T_g$  in  $\text{SmB}_6$ . The skin depth  $\delta = \sqrt{\rho/\pi\nu\mu}$ , where  $\mu = \mu_0(1 + \chi)$ , depends on  $\nu$  as well as  $T$ -dependent  $\rho$  and  $\chi$  of the sample. For  $\text{SmB}_6$ , using our measured values of bulk resistivity  $\rho = 10^{-3} \Omega \text{ cm}$  [Fig. 2(a)] and  $\chi = 10.1 \times 10^{-3}$  at 100 K (Sec. VI in the

Supplemental Material [50]), we estimate  $\delta_{\text{SmB}_6}(100 \text{ K}) \sim 25 \text{ nm}$  at  $\nu = 4 \text{ kHz}$ . Note that  $V'(T) \propto \Lambda(T)$ , with  $\Lambda(T) \sim s\delta(T)$ , where  $\Lambda$  is the effective sample volume which is being probed by the penetrating electromagnetic signal, and  $s$  is the surface area of the sample. Note that  $\Lambda$  has the same  $T$  dependence as  $\delta$ . At 100 K, the  $V'$  response is from the entire bulk of the sample. For  $\text{SmB}_6$ , the estimated  $\delta(100 \text{ K}) \sim 25 \text{ nm}$  at 100 K is much greater than the sample thickness,  $t$  of 200  $\mu\text{m}$ ; therefore, at 100 K,  $\Lambda(100 \text{ K}) = st$ . Using  $V'(T) \propto \Lambda(T)$  for  $\text{SmB}_6$ , we estimate at  $\nu = 4 \text{ kHz}$ ,  $\delta_{\text{SmB}_6}(40 \text{ K}) = \frac{V'(40 \text{ K})}{V'(100 \text{ K})} \times t = 4.7 \mu\text{m}$ , where  $V'(T)$  are the directly measured values. Note the above method for estimating  $\delta_{\text{SmB}_6}$  works down to the  $T$  regime of 40 K, where there is a dominant bulk contribution to electrical conductivity. Below 40 K, the onset of a higher-conductivity surface layer in  $\text{SmB}_6$  ( $[A-BT]$  dependence of  $V'(T)$ ) screens the probing signal from most of the bulk. Therefore,  $< 40$  K, to estimate  $\delta$ , we consider surface conductivity  $\sigma_s(T) = \sigma_{0s}(A-BT)$ , where  $\sigma_{0s}$  is a constant  $T$ -independent proportionality factor, and  $A$ ,  $B$  values are determined from the linear fit to the effective conductivity response of  $\text{SmB}_6$  at 4 kHz [see Fig. 3(a)]. Using  $\delta = \delta_0 \sqrt{\frac{\sigma_0}{\sigma_s(T)}}$ , where  $\delta_0 = \delta_{\text{SmB}_6}(40 \text{ K})$  and  $\sigma_0 = \sigma_{\text{SmB}_6}^{40 \text{ K}}$ , we estimate  $\delta \sim 400 \text{ nm} < 25 \text{ K}$  (see Sec. XII in the Supplemental Material [50] for detailed calculation and plot of  $T$  dependence of estimated  $\delta$  for  $\text{SmB}_6$  and  $\text{Bi}_2\text{Se}_3$ ). Therefore, in  $\text{SmB}_6$  for a 4 kHz pick-up measurement at low  $T$ , the contribution to the pick-up signal is predominantly from  $\sim 400 \text{ nm}$ -thick surface layer. Hence, the thin, high-conducting surface layer we are probing at  $T < T_g$  is of submicron-order thickness. Here, we would like to mention that we have not polished any of our crystal faces before any of our pick-up coil measurements. Also note that the behavior of  $V'(T)$  around  $T_g$  does not change significantly for measurements done at higher  $\nu$  (see plot of  $V'(T)$  at  $\nu = 4, 8, 12$ , and 55 kHz in Sec. IX in the Supplemental Material [50]).

Electrical transport studies in  $\text{SmB}_6$  thin films [64,65] suggest surface conducting features appear only  $< 10$  K. It is known that, in electrical transport measurements, there is mixing of the surface and bulk conductivities in the net measured conductivity due to parallel transport channels through the bulk and surface. Disentangling and determining the two contributions is a fairly complex issue in such measurements. Here, only at very low  $T$  (4 K and below), as the conducting channels through the bulk become almost open due to high resistance, especially in  $\text{SmB}_6$ , does one begin to observe the surface contribution to electrical conductivity. Due to these complications, it may not always be possible to determine at what  $T$  the onset of surface conductivity occurs in electrical transport measurements. However, in our  $\nu$ -dependent pick-up coil technique, we see the presence of a thin, high-conducting surface layer appearing at  $T < T_g$  in  $\text{SmB}_6$ .

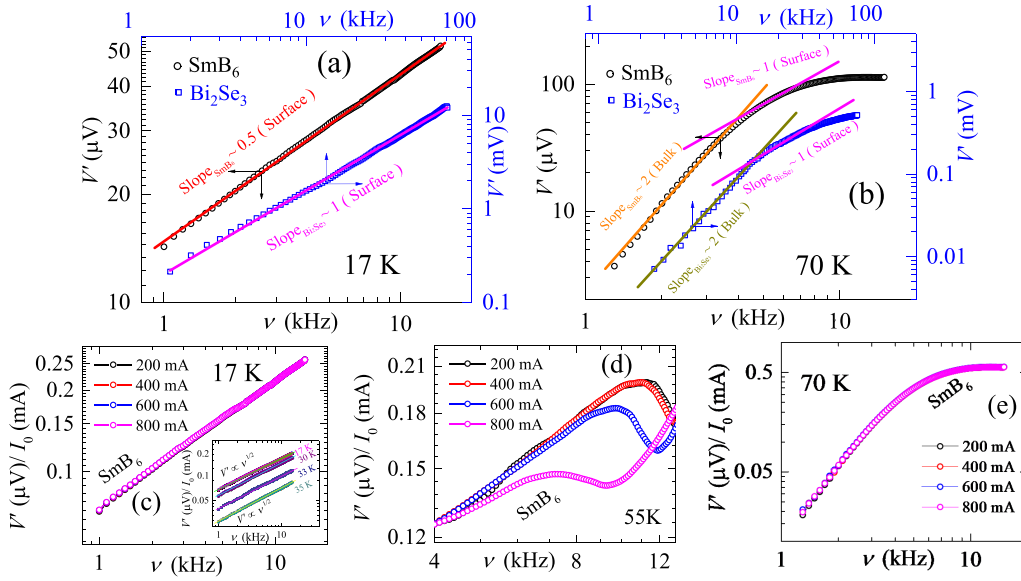


FIG. 4. Excitation frequency and  $I_0$  dependence of the pick-up signal of  $\text{SmB}_6$  and  $\text{Bi}_2\text{Se}_3$  at different  $T$ . (a) shows the log-log plot of  $V'(\nu)$  response of  $\text{Bi}_2\text{Se}_3$  (blue open squares) and  $\text{SmB}_6$  (black open circles) at 17 K. Red and magenta solid lines indicate  $V' \propto \nu^{1/2}$  and  $V' \propto \nu$  response of sample  $\text{SmB}_6$  and  $\text{Bi}_2\text{Se}_3$ , respectively. (b) shows the log-log plot of  $V'(\nu)$  response of  $\text{Bi}_2\text{Se}_3$  (blue open squares) and  $\text{SmB}_6$  (black open circles) at 70 K. Orange and dark yellow solid lines indicate  $V' \propto \nu^2$  response of both samples  $\text{SmB}_6$  and  $\text{Bi}_2\text{Se}_3$ , respectively. Magenta solid lines indicate  $V' \propto \nu$  response of both samples  $\text{SmB}_6$  and  $\text{Bi}_2\text{Se}_3$ . (c) shows the scaled behavior of  $V'(\nu)$  response of  $\text{SmB}_6$  at 17 K for different excitation currents ( $I_0$ ). Inset shows the scaled behavior of  $V' \propto \nu^{1/2}$  seen at different  $T$  of 17, 30, 33, and 35 K, below  $T_g = 40$  K. Note that, at each  $T$ ,  $V'(\nu)$  is measured with different excitation amplitude  $I_0$  and then normalized  $V'/I_0$  data are plotted vs  $\nu$ . (d) shows the nonscaled nature of  $V'(\nu)$  response of  $\text{SmB}_6$  at 55 K for different excitation currents. (e) shows the scaled behavior of  $V'(\nu)$  response of  $\text{SmB}_6$  at 70 K for different excitation currents. Note that the excitation current values shown in the figures correspond to the peak value ( $I_0$ ) of the AC current in the primary excitation coil.

#### D. Comparison of $V'(\nu)$ response of $\text{Bi}_2\text{Se}_3$ and $\text{SmB}_6$ with different $I_0$ at different $T$

It may be recalled here that the skin depth becomes small at higher  $\nu$ ; therefore,  $\nu$  studies are useful to discern between the bulk and surface layer conducting properties. Here, we study the frequency dependence of  $V'$  to explore the properties of the thin, high-conducting surface layer in  $\text{SmB}_6$ . Authors of studies on the frequency dependence of  $V'$  in TI material like  $\text{Bi}_2\text{Se}_3$  [42,43] have shown that, at low  $T$ , viz., in the  $\sigma_s$ -dominated regime,  $V'(\nu) \propto \nu^\alpha$ , where  $\alpha \sim 1$ , while in the high- $T$  regime ( $> 70$  K), where  $\sigma_b$  dominates,  $\alpha \sim 2$ . Figure 4(a) shows the  $V'(\nu)$  response on a log-log scale for both  $\text{SmB}_6$  and  $\text{Bi}_2\text{Se}_3$  at 17 K, measured with a peak amplitude of the excitation current ( $I_0$ ) = 200 mA in the primary excitation coil. Here, the linear nature of  $V'(\nu)$  with slope of  $0.976 \pm 0.003$  for  $\text{Bi}_2\text{Se}_3$  suggests  $V' \propto \nu$  (see magenta line). However, for  $\text{SmB}_6$  at  $T = 17$  K, which is below  $T_g$ , we observe  $V' \propto \nu^{1/2}$  [slope of red line in Fig. 4(a) is  $0.464 \pm 0.001$ ]. The  $\nu$  dependence of  $V'(\nu)$  in this low- $T$  regime is strikingly different in the two materials. The inset of Fig. 4(c) shows multiple datasets confirming the  $V'(\nu) \propto \nu^{1/2}$  behavior at different  $T$ 's of 17, 30, and 35 K, below  $T_g = 40$  K in  $\text{SmB}_6$  (also see Sec. X in the Supplemental Material [50] for more  $T$  data). Figure 4(b) compares the  $V'(\nu)$  response for  $I_0 = 200$  mA of  $\text{SmB}_6$  and  $\text{Bi}_2\text{Se}_3$  at 70 K (viz., at  $T > T_g$  for  $\text{SmB}_6$  and inside the bulk conducting regime for  $\text{Bi}_2\text{Se}_3$ ). We note that, in the log-log plot of  $V'(\nu)$ ,  $\text{Bi}_2\text{Se}_3$  has a slope  $1.838 \pm 0.0742$  (dark yellow line) which is nearly like that for  $\text{SmB}_6$  showing a slope of  $2.014 \pm 0.041$  (orange line).

This suggests  $V' \propto \nu^2$  in the low- $\nu$  regime for both materials. For higher  $\nu$  at 70 K, we observe  $V'(\nu) \propto \nu$  behavior in both  $\text{Bi}_2\text{Se}_3$  and  $\text{SmB}_6$  [magenta lines in Fig. 4(b)]. In  $\text{Bi}_2\text{Se}_3$  at high  $T$ , the dominance of bulk contribution to conductivity leads to  $V' \propto \nu^2$  in the low- $\nu$  regime, while at higher  $\nu$ , the dominance of surface contribution to conductivity leads to  $V'(\nu) \propto \nu$  [42]. Recall that authors of studies in  $\text{Bi}_2\text{Se}_3$  showed that linear frequency dependence of  $V'(\nu)$  is a characterizing feature of the conducting surface state in a noninteracting conventional TI material like  $\text{Bi}_2\text{Se}_3$  [38,42]. In  $\text{SmB}_6$ ,  $V'(\nu) \propto \nu^2$  in the low- $\nu$  regime at 70 K is related to dominant bulk contribution to conductivity. In the high- $T$  regime of 70 K ( $> T_g$ ), as bulk contributions to conductivity are admixed with surface conductivity features, for  $\text{SmB}_6$ , it is difficult to discern  $V'(\nu) \propto \nu$  from  $\nu^{1/2}$  dependence. Note that correlations have not started to develop until below  $T^*$  in  $\text{SmB}_6$ . Only at temperatures below  $T_g$ , where the bulk contribution to conductivity diminishes significantly, is the unique  $V'(\nu) \propto \nu^{1/2}$  behavior for  $\text{SmB}_6$  seen. The  $V'(\nu) \propto \nu^{1/2}$  is a characteristic feature of the thin, high-conducting surface layer emerging below  $T_g$  in  $\text{SmB}_6$ . In the discussion section, we discuss a possible scenario for this unique  $\nu$  dependence of  $V'(\nu)$  in  $\text{SmB}_6$ . At  $T = 70$  K, we estimate the relative fraction of bulk ( $P_b$ ) and surface ( $P_s$ ) contributions to  $V'(\nu)$  by fitting it to  $V'(\nu) = P_b[V'_b(\nu)] + P_s[V'_s(\nu)]$ , where  $V'_b(\nu)$  and  $V'_s(\nu)$  are the pick-up response from the bulk and surface, respectively. The data fit well only in a limited frequency window where both the surface [ $V'_s(\nu) \propto \nu$ ] and bulk [ $V'_b(\nu) \propto \nu^2$ ] contributions are present in the behavior of  $V'(\nu)$  (see Sec. XIII in the

Supplemental Material [50]). At 70 K, the fit yields for  $\text{SmB}_6$   $P_b = 70\%$  and  $P_s = 30\%$ , whereas for  $\text{Bi}_2\text{Se}_3$ ,  $P_b = 51\%$  and  $P_s = 49\%$ . It may be noted that, using this analysis, the values for  $P_b$  and  $P_s$  we obtain for  $\text{Bi}_2\text{Se}_3$  at 70 K are consistent with those reported earlier [42].

Recall that the AC field from the excitation coil which the sample experiences is proportional to the amplitude of the AC current ( $I_0$ ) in the excitation coil. We plot  $\frac{V'}{I_0}$  vs  $\nu$  in Figs. 4(c)–4(e) for different  $I_0$  and at  $T$  values chosen in regimes labeled (iii), (ii), and (i) from Fig. 1(f), respectively. The  $V'(\nu)$  signal scales with  $I_0$  in regime (iii), i.e.,  $T \ll T_g$  [Fig. 4(c)], and in regime (i), i.e.,  $T > T^*$  [see Fig. 4(e)]. The inset of Fig. 4(c) shows the scaled behavior of  $V'(\nu)$  for different  $I_0$  at different  $T$  below  $T_g$ . However, in regime (ii),  $T_g < T < T^*$  [see Fig. 4(d)] for  $I_0 < 600$  mA, the data scale up to  $\nu < 8$  kHz. At  $\nu > 8$  kHz, as seen in Fig. 4(d),  $V'(\nu)$  deviates from the scaled curve, with  $\frac{V'}{I_0}$  declining and reaching minima before resuming its increasing trend at higher  $\nu$ . The departure from scaling increases as  $I_0$  increases. The above suggests a significant nonlinear response with varying amplitude of the AC excitation current in regime (ii), viz.,  $T_g < T < T^*$ . In this regime,  $V'(\nu)$  drops rather than increasing with  $\nu$  in the range of 8–12 kHz, as seen in Fig. 4(d). This nonlinear response cannot be attributed to the heating of the sample because then it would have been present in all three  $T$  regimes. Furthermore, our noncontact measurement technique restricts any kind of contact heating (see Sec. XIV in the Supplemental Material [50]) and thus ensures the nonlinear response coming inherently from the sample itself.

#### IV. DISCUSSION

Our measurements in  $\text{SmB}_6$  enable us to distinguish between three distinct  $T$  regimes, viz., (i)  $T \geq T^*$  ( $\sim 66$  K), (ii) ( $\sim 40$  K)  $T_g \leq T < T^*$ , and (iii)  $T < T_g$ . Our  $\chi(T)$  measurements in regime (i) show the presence of Curie-Weiss behavior with no magnetic ordering. In the  $T$  regime (ii), i.e., below  $T^*$ , the strong correlation effects start to develop, and they play an important role in shaping the properties of  $\text{SmB}_6$ . Near  $T^*$ , both DC magnetization [see Fig. 2(b) inset] and our AC two-coil pick-up measurements [see Fig. 1(f)] show noticeable change in curvature as a result of Kondo screening, and a weak bumplike feature in  $\frac{d\rho}{dT}$  is found in electrical transport measurements (see Sec. V in the Supplemental Material [50]). The two-coil pick-up signal noticeably drops in regime (ii) and reaches its minimum value at  $T_g$ . In regime (iii), despite the large increase in the bulk resistivity below  $T_g$ , our two-coil pick-up signal recovers, revealing that the material possesses a thin surface layer of submicron thickness with high conductivity. It is worth noting that, below  $T_g$ , the bulk conductivity of the sample diminishes significantly. We observe a distinctive sublinear frequency dependence of the pick-up signal in this  $T$  regime (iii), i.e.,  $V'(\nu) \propto \nu^{1/2}$ . Here, we also find a dominant linear  $T$  dependence of the pick-up signal, suggesting strong correlation governing the behavior of surface electrical conductivity below  $T_g$ . We find that the pick-up response scales with the drive (excitation) amplitude at  $T < T_g$  and at  $T > T^*$  [see Figs. 4(c) and 4(e)], whereas in between  $T_g$  and  $T^*$ , there is a nonscaled regime [see Fig. 4(d)]. To understand the scattering mechanism

governing electrical transport in regime (i) ( $T \geq T^*$ ), we approximate the behavior of  $\rho(T)$  using a conventional Hamann function [see Fig. 2(a) main panel and inset (I)] of the form  $\rho(T) = \rho_{K0} \left[ 1 - \frac{\ln(T/T_K)}{\sqrt{\ln^2(T/T_K) + s(s+1)\pi^2}} \right] + \rho_0$ , where  $T_K$  is the Kondo temperature scale,  $s$  is the spin of the magnetic impurity,  $\rho_{K0}$  is the proportionality constant, and  $\rho_0$  is the residual resistivity [56]. The data in Fig. 2(a) inset (I) fit to this function from high  $T$  to  $T^*$  with fitting parameters  $T_K = 7.80 \pm 0.91$  K,  $s = 2.4 \pm 0.1$ ,  $\rho_{K0} = 0.00801 \pm 0.00009$   $\Omega$  cm, and  $\rho_0 = 0.00229 \pm 0.00004$   $\Omega$  cm. The low- $T_K$  value suggests weak exchange interaction between conduction electrons with a dilute density of uncorrelated magnetized impurities. Below  $T^*$ , the deviation of the measured  $\rho(T)$  from the Hamann function fit shows a failure of single-impurity model in regime (ii). In regime (ii) at  $T < T^*$ , there is a gradual onset of Kondo hybridization between the Sm ion moments and the itinerant electrons in  $\text{SmB}_6$ , and one can no longer consider the magnetic ions as dilute, i.e., independent. Below  $T^*$  at  $T_g = 40$  K, a uniform Kondo gap develops across the bulk of the sample. We recall here that earlier transport measurements in  $\text{SmB}_6$  [4,5,14,15,54] also reported seeing a bulk Kondo gap-opening temperature in the range of 30–50 K, which is consistent with our  $T_g$  value of 40 K. It is interesting to note here that, contrary to us, authors of earlier transport studies have suggested the presence of a high-conducting state only at very low  $T$ , typically well below 10 K. In the context of our regime (ii), scanning tunneling spectroscopy (STS) measurements in  $\text{SmB}_6$  [55] showed suppression in the density of states and a gaplike feature emerging in their spectra from  $\sim 60$  K, which is like our  $T^*$  scale. The STS spectra show an evolution with lowering of  $T$ . The gaplike feature which begins developing from 60 K becomes a robust Kondo hybridization gap at 40 K, which is like our  $T_g$ . Furthermore, like our study, from point contact spectroscopy, one can also identify three different temperature regimes [23]. At  $T > 90$  K, the highly symmetric conductance spectra with negligible  $T$  dependence is marked as the regime of weak interaction between the electrons and the local moments [23]. The temperature range of 90–30 K is described as a single-ion resonance regime where the zero bias conductance is suppressed, and asymmetry starts to develop in the conductance spectra. Below 30 K, the highly asymmetric conductance spectra suggest the emergence of Kondo hybridization due to strong correlation [23]. Here, our regime (i) is consistent with the weak interaction regime reported in the spectroscopy studies [23]. In regime (ii), i.e.,  $T_g \leq T < T^*$ , the strong  $f$ - $d$  exchange interaction at Sm ion sites dominates over the weaker electron-impurity ion exchange interaction (which is present above  $T^*$ ). We would like to mention that there may be a mismatch between our temperature scales and those reported in the literature [1,5,15,23,30,55], which is due to differences in sample quality that affect the location of the temperature scales. With the bulk fully gapped at  $T_g$ , we see the presence of a thin, high-conducting surface layer contribution to conductivity in the vicinity of  $T_g$  in our pick-up coil measurements. It is interesting to note here that ARPES in  $\text{SmB}_6$  [20] showed dispersive states which are of surface origin within the Kondo hybridization gap. A well-formed Kondo gap feature is seen at 40 K, which is like our  $T_g$  value. ARPES [20] further suggested that these states may be present even at  $T > 40$  K.

It also indicated that these states with surface origin possess chirality of the orbital angular momentum [20]. In this paper, we imply that the thin surface layer we observe at  $T < T_g$  possesses high surface conductivity. Strong correlation effects modify the scattering, leading to observed linear  $T$  dependence of the surface conductivity below  $T_g$ .

We discuss here a few possible scenarios related to the observed  $T$  and  $\nu$  dependence of  $V'$  in  $\text{SmB}_6$  below  $T_g$ . The total AC conductivity  $\sigma_{\text{total}}(\omega = 2\pi\nu) = \sigma_{\text{DS}}(\omega) + \sigma_{e-e}(\omega)$ , where  $\sigma_{\text{DS}}(\omega) = \frac{\sigma_0}{(1-i\omega\tau)} [1 + \sum_{n=1}^{\infty} \frac{c_n}{(1-i\omega\tau)^n}]$  is the Drude-Smith (DS) conductivity which also considers the effect of multiple scattering events on the conductivity [66,67],  $\sigma_0$  is the conventional Drude DC conductivity,  $\tau$  is the time interval between two consecutive scattering,  $c_n$  represents the fraction of the original velocity of the carrier that is retained after the  $n$ th scattering ( $n$  is an integer), and  $\sigma_{e-e}(\omega)$  is the conductivity in the presence of strong electron-electron interaction effects. The first term in  $\sigma_{\text{DS}}(\omega)$  is  $\sigma_D(\omega)$ . Note that higher-order contributions from scattering ( $n \geq 1$ ) in  $\sigma_{\text{DS}}(\omega)$  have progressively decreasing weights and consequently much weaker contribution to the surface conductivity. While the linear  $\nu$  dependence of  $V'$  at low  $T$  in  $\text{Bi}_2\text{Se}_3$  was explained earlier [42] by considering topological surface state contributions (viz.,  $\omega\tau \gg 1$ ) to the leading-order term in  $\sigma_{\text{DS}}(\omega)$ ,  $V' \propto \nu^{1/2}$  behavior in  $\text{SmB}_6$  below  $T_g$  cannot be explained by the higher-order terms in  $\sigma_{\text{DS}}(\omega)$  alone. In this context, one possible scenario to consider is the effect of strong  $e-e$  interactions [68–71], which are known to produce nonintegral  $\nu$  dependence of  $\sigma_{e-e}(\omega = 2\pi\nu)$  of the type  $\sigma_{e-e}(\omega) \propto [\ln(\frac{2\hbar}{\hbar\omega})]^3 (\frac{\omega}{\epsilon})$ . At  $T < T_g$ , we observe a noninteger exponent in the  $\nu$  dependence of  $V'$ , viz.,  $V' \propto \nu^{1/2}$ . Concomitantly, below  $T_g$ , we also observe unusual  $[A-BT]$  behavior in  $V'(T)$ . It is possible that, in  $\text{SmB}_6$ , these features are associated with emergence of a high-conducting surface layer [9,14,23,28,72–74] together with strong  $f-f$  electron correlations effects. We would like to mention that the above is suggested as a probable scenario. These results suggest the need for further theoretical investigations to explore mechanisms related to  $\nu^{1/2}$  behavior. In our  $T$  regime (ii), which is between  $T^*$  and  $T_g$ , it is likely that the interplay of the emerging bulk Kondo hybridized state and the emerging highly conductive strongly

correlated surface layer conductivity results in the observed nonscaling behavior of  $V'(\nu)/I_0$  [cf. Fig. 4(d)]. Our findings and the discussion above lead us to consider that  $\text{SmB}_6$  has signatures of weak interactions above  $T^*$ , where the transport is dominated by scattering from dilute magnetic ions. At  $T < T^*$ , a strongly correlated Kondo hybridization state between the localized Sm ion moments and the itinerant electrons progressively takes hold. At  $T_g$ , a Kondo hybridization gap uniformly opens throughout most of the sample. It is probable that the strongly correlated surface layer response is present above  $T_g$ , and it begins to affect the conductivity of  $\text{SmB}_6$  between  $T^*$  and  $T_g$ . However, we clearly detect the emergence of a thin, high-conducting surface layer in  $\text{SmB}_6$  from just below  $T_g$  when the bulk electrical conductivity rapidly diminishes due to the opening of the Kondo gap in bulk of the material.

## V. CONCLUSIONS

In conclusion, through careful comparison with a conventional TI material  $\text{Bi}_2\text{Se}_3$ , we identify three distinct temperature regimes of bulk Kondo gap formation in  $\text{SmB}_6$ . The process sets in from below a temperature scale  $T^*$ , and the uniform gap appears across the entire bulk only below  $T_g$ . Simultaneously, in the vicinity of  $T_g$ , the features of a strongly correlated thin, high-conducting surface layer begin to emerge in  $\text{SmB}_6$ . More detailed experimental and theoretical investigations are needed in the future to probe these regimes in strongly interacting TI materials.

## ACKNOWLEDGMENTS

The authors thank Priscila F. S. Rosa (Los Alamos National Laboratory) and A. Bharathi (UGC-DAE Consortium for Scientific Research) for single crystals. We also thank P. F. S. Rosa and S. M. Thomas for private communication and fruitful discussions. S.S.B. thanks funding support from DST-SERB (SUPRA), DST-AMT, and IIT Kanpur. S.G. thanks Council of Scientific and Industrial Research, India for funding support. S.P. thanks the Prime Minister's Research Fellowship (PMRF, scheme code 3268) of the Ministry of Human Resource Development, Government of India, for funding support.

- 
- [1] Z. Fisk, J. L. Sarrao, S. L. Cooper, P. Nyhus, G. S. Boebinger, A. Passner, and P. C. Canfield, *Physica B* **223**, 409 (1996).  
 [2] R. M. Martin and J. W. Allen, *J. Appl. Phys.* **50**, 7561 (1979).  
 [3] H. Tsunetsugu, M. Sigrist, and K. Ueda, *Rev. Mod. Phys.* **69**, 809 (1997).  
 [4] A. Menth, E. Buehler, and T. H. Geballe, *Phys. Rev. Lett.* **22**, 295 (1969).  
 [5] J. W. Allen, B. Batlogg, and P. Wachter, *Phys. Rev. B* **20**, 4807 (1979).  
 [6] J. C. Cooley, M. C. Aronson, Z. Fisk, and P. C. Canfield, *Phys. Rev. Lett.* **74**, 1629 (1995).  
 [7] M. Dzero, J. Xia, V. Galitski, and P. Coleman, *Annu. Rev. Condens. Matter Phys.* **7**, 249 (2016).  
 [8] M. Dzero, K. Sun, P. Coleman, and V. Galitski, *Phys. Rev. B* **85**, 045130 (2012).  
 [9] M. Dzero, K. Sun, V. Galitski, and P. Coleman, *Phys. Rev. Lett.* **104**, 106408 (2010).  
 [10] C. L. Kane and E. J. Mele, *Phys. Rev. Lett.* **95**, 226801 (2005).  
 [11] C. L. Kane and E. J. Mele, *Phys. Rev. Lett.* **95**, 146802 (2005).  
 [12] B. A. Bernevig, T. L. Hughes, and S.-C. Zhang, *Science* **314**, 1757 (2006).  
 [13] M. Z. Hasan and C. L. Kane, *Rev. Mod. Phys.* **82**, 3045 (2010).  
 [14] S. Wolgast, Ç. Kurdak, K. Sun, J. W. Allen, D.-J. Kim, and Z. Fisk, *Phys. Rev. B* **88**, 180405(R) (2013).  
 [15] D. J. Kim, S. Thomas, T. Grant, J. Botimer, Z. Fisk, and J. Xia, *Sci. Rep.* **3**, 3150 (2013).  
 [16] P. Syers, D. Kim, M. S. Fuhrer, and J. Paglione, *Phys. Rev. Lett.* **114**, 096601 (2015).

- [17] Y. S. Eo, A. Rakoski, J. Lucien, D. Mihaliiov, Ç. Kurdak, P. F. S. Rosa, and Z. Fisk, *Proc. Natl. Acad. Sci. USA* **116**, 12638 (2019).
- [18] H. Miyazaki, T. Hajiri, T. Ito, S. Kunii, and S.-i. Kimura, *Phys. Rev. B* **86**, 075105 (2012).
- [19] Y. Xu, I. Miotkowski, C. Liu, J. Tian, H. Nam, N. Alidoust, J. Hu, C. K. Shih, M. Z. Hasan, and Y. P. Chen, *Nat. Phys.* **10**, 956 (2014).
- [20] J. Jiang, S. Li, T. Zhang, Z. Sun, F. Chen, Z. R. Ye, M. Xu, Q. Q. Ge, S. Y. Tan, X. H. Niu *et al.*, *Nat. Commun.* **4**, 3010 (2013).
- [21] E. Frantzeskakis, N. de Jong, B. Zwartsenberg, Y. K. Huang, Y. Pan, X. Zhang, J. X. Zhang, F. X. Zhang, L. H. Bao, O. Tegus *et al.*, *Phys. Rev. X* **3**, 041024 (2013).
- [22] W. T. Fuhrman, J. Leiner, P. Nikolić, G. E. Granroth, M. B. Stone, M. D. Lumsden, L. DeBeer-Schmitt, P. A. Alekseev, J. M. Mignot, S. M. Koohpayeh *et al.*, *Phys. Rev. Lett.* **114**, 036401 (2015).
- [23] X. Zhang, N. P. Butch, P. Syers, S. Ziemak, R. L. Greene, and J. Paglione, *Phys. Rev. X* **3**, 011011 (2013).
- [24] G. Li, Z. Xiang, F. Yu, T. Asaba, B. Lawson, P. Cai, C. Tinsman, A. Berkley, S. Wolgast, Y. S. Eo *et al.*, *Science* **346**, 1208 (2014).
- [25] S. M. Thomas, X. Ding, F. Ronning, V. Zapf, J. D. Thompson, Z. Fisk, J. Xia, and P. F. S. Rosa, *Phys. Rev. Lett.* **122**, 166401 (2019).
- [26] B. S. Tan, Y.-T. Hsu, B. Zeng, M. Ciomaga Hatnean, N. Harrison, Z. Zhu, M. Hartstein, M. Kiourlappou, A. Srivastava, M. D. Johannes *et al.*, *Science* **349**, 287 (2015).
- [27] M. Hartstein, W. H. Toews, Y.-T. Hsu, B. Zeng, X. Chen, M. Ciomaga Hatnean, Q. R. Zhang, S. Nakamura, A. S. Padgett, G. Rodway-Gant *et al.*, *Nat. Phys.* **14**, 166 (2018).
- [28] M. Neupane, N. Alidoust, S.-Y. Xu, T. Kondo, Y. Ishida, D. J. Kim, Chang Liu, I. Belopolski, Y. J. Jo, T.-R. Chang *et al.*, *Nat. Commun.* **4**, 2991 (2013).
- [29] N. Xu, C. E. Matt, E. Pomjakushina, X. Shi, R. S. Dhaka, N. C. Plumb, M. Radović, P. K. Biswas, D. Evtushinsky, V. Zabolotny *et al.*, *Phys. Rev. B* **90**, 085148 (2014).
- [30] H. Pirie, Y. Liu, A. Soumyanarayanan, P. Chen, Y. He, M. M. Yee, P. F. S. Rosa, J. D. Thompson, D. Kim, Z. Fisk *et al.*, *Nat. Phys.* **16**, 52 (2020).
- [31] B. Roy, J. D. Sau, M. Dzero, and V. Galitski, *Phys. Rev. B* **90**, 155314 (2014).
- [32] P. Nikolić, *Phys. Rev. B* **90**, 235107 (2014).
- [33] W. T. Fuhrman and P. Nikolić, *Phys. Rev. B* **90**, 195144 (2014).
- [34] L. Li, K. Sun, C. Kurdak, and J. W. Allen, *Nat. Rev. Phys.* **2**, 463 (2020).
- [35] P. F. S. Rosa and Z. Fisk, *Bulk and Surface Properties of SmB<sub>6</sub>, Rare-Earth Borides*, 1st ed. (Jenny Stanford Publishing, New York, 2021), Chap. 11.
- [36] D.-X. Qu, Y. S. Hor, J. Xiong, R. J. Cava, and N. P. Ong, *Science* **329**, 821 (2010).
- [37] L. A. Jauregui, M. T. Pettes, L. P. Rokhinson, L. Shi, and Y. P. Chen, *Sci. Rep.* **5**, 8452 (2015).
- [38] B. F. Gao, P. Gehring, M. Burghard, and K. Kern, *Appl. Phys. Lett.* **100**, 212402 (2012).
- [39] Y. S. Kim, M. Brahlek, N. Bansal, E. Edrey, G. A. Kapilevich, K. Iida, M. Tanimura, Y. Horibe, S.-W. Cheong, and S. Oh, *Phys. Rev. B* **84**, 073109 (2011).
- [40] T. R. Devidas, E. P. Amaladass, S. Sharma, R. Rajaraman, D. Sornadurai, N. Subramanian, A. Mani, C. S. Sundar, and A. Bharathi, *EPL* **108**, 67008 (2014).
- [41] E. P. Amaladass, T. R. Devidas, S. Sharma, C. S. Sundar, A. Mani, and A. Bharathi, *J. Phys. Condens. Matter* **28**, 075003 (2016).
- [42] A. Jash, K. Nath, T. R. Devidas, A. Bharathi, and S. S. Banerjee, *Phys. Rev. Appl.* **12**, 014056 (2019).
- [43] A. Jash, S. Ghosh, A. Bharathi, and S. S. Banerjee, *Phys. Rev. B* **101**, 165119 (2020).
- [44] A. F. Hebard and A. T. Fiory, *Phys. Rev. Lett.* **44**, 291 (1980).
- [45] A. T. Fiory, A. F. Hebard, P. M. Mankiewich, and R. E. Howard, *Appl. Phys. Lett.* **52**, 2165 (1988).
- [46] J. H. Claassen, M. L. Wilson, J. M. Byers, and S. Adrian, *J. Appl. Phys.* **82**, 3028 (1997).
- [47] X. He, A. Gozar, R. Sundling, and I. Božović, *Rev. Sci. Instrum.* **87**, 113903 (2016).
- [48] X.-L. Qi and S.-C. Zhang, *Rev. Mod. Phys.* **83**, 1057 (2011).
- [49] H. Zhang, C.-X. Liu, X.-L. Qi, X. Dai, Z. Fang, and S.-C. Zhang, *Nat. Phys.* **5**, 438 (2009).
- [50] See Supplemental Material at <http://link.aps.org/supplemental/10.1103/PhysRevB.108.205101> for more experimental details and characterization, which includes Refs. [75,76].
- [51] T. R. Devidas, E. P. Amaladass, S. Sharma, A. Mani, R. Rajaraman, C. S. Sundar, and A. Bharathi, *Mater. Res. Express* **4**, 026101 (2017).
- [52] A. Jash, S. Ghosh, A. Bharathi, and S. S. Banerjee, *Bull. Mater. Sci.* **45**, 17 (2022).
- [53] H. M. Benia, C. Lin, K. Kern, and C. R. Ast, *Phys. Rev. Lett.* **107**, 177602 (2011).
- [54] J. Roman, V. Pavlík, K. Flachbart, T. Herrmannsdörfer, S. Rehmman, E. S. Konovalova, and Y. B. Paderno, *Physica B* **230**, 715 (1997).
- [55] W. Ruan, C. Ye, M. Guo, F. Chen, X. Chen, G.-M. Zhang, and Y. Wang, *Phys. Rev. Lett.* **112**, 136401 (2014).
- [56] D. R. Hamann, *Phys. Rev.* **158**, 570 (1967).
- [57] P. K. Biswas, Z. Salman, T. Neupert, E. Morenzoni, E. Pomjakushina, F. von Rohr, K. Conder, G. Balakrishnan, M. Ciomaga Hatnean, M. R. Lees *et al.*, *Phys. Rev. B* **89**, 161107(R) (2014).
- [58] W. T. Fuhrman, J. C. Leiner, J. W. Freeland, M. van Veenendaal, S. M. Koohpayeh, W. A. Phelan, T. M. McQueen, and C. Broholm, *Phys. Rev. B* **99**, 020401(R) (2019).
- [59] S. Kondo, D. C. Johnston, C. A. Swenson, F. Borsa, A. V. Mahajan, L. L. Miller, T. Gu, A. I. Goldman, M. B. Maple, D. A. Gajewski *et al.*, *Phys. Rev. Lett.* **78**, 3729 (1997).
- [60] J. M. Tomczak, K. Haule, and G. Kotliar, *Proc. Natl. Acad. Sci. USA* **109**, 3243 (2012).
- [61] I. A. Nekrasov, Z. V. Pchelkina, G. Keller, T. Pruschke, K. Held, A. Krimmel, D. Vollhardt, and V. I. Anisimov, *Phys. Rev. B* **67**, 085111 (2003).
- [62] D. Kim, Q. Li, P. Syers, N. P. Butch, J. Paglione, S. Das Sarma, and M. S. Fuhrer, *Phys. Rev. Lett.* **109**, 166801 (2012).
- [63] Z. Ren, A. A. Taskin, S. Sasaki, K. Segawa, and Y. Ando, *Phys. Rev. B* **82**, 241306(R) (2010).
- [64] T. Liu, Y. Li, L. Gu, J. Ding, H. Chang, P. A. Praveen Janantha, B. Kalinikos, V. Novosad, A. Hoffmann, R. Wu *et al.*, *Phys. Rev. Lett.* **120**, 207206 (2018).

- [65] S. Lee, X. Zhang, Y. Liang, S. W. Fackler, J. Yong, X. Wang, J. Paglione, R. L. Greene, and I. Takeuchi, [Phys. Rev. X](#) **6**, 031031 (2016).
- [66] N. V. Smith, [Phys. Rev. B](#) **64**, 155106 (2001).
- [67] K. Shimakawa and S. Kasap, [Appl. Sci.](#) **6**, 50 (2016).
- [68] J. C. Dyre and T. B. Schröder, [Rev. Mod. Phys.](#) **72**, 873 (2000).
- [69] *Electronic Processes in Non-Crystalline Materials*, edited by N. F. Mott and E. A. Davis (Oxford University Press, Oxford, 1979).
- [70] N. J. Laurita, C. M. Morris, S. M. Koohpayeh, W. A. Phelan, T. M. McQueen, and N. P. Armitage, [Physica B](#) **536**, 78 (2018).
- [71] B. I. Shklovskii and A. L. Efros, [Sov. Phys. JETP](#) **54**, 218 (1981).
- [72] A. A. Soluyanov and D. Vanderbilt, [Phys. Rev. B](#) **83**, 035108 (2011).
- [73] T. Takimoto, [J. Phys. Soc. Jpn.](#) **80**, 123710 (2011).
- [74] D. J. Kim, T. Grant, and Z. Fisk, [Phys. Rev. Lett.](#) **109**, 096601 (2012).
- [75] M. C. Hatnean, M. R. Lees, D. M. Paul, and G. Balakrishnan, [Sci. Rep.](#) **3**, 3071 (2013).
- [76] L. J. Berchmans, A. Visuvasam, S. Angappan, C. Subramanian, and A. K. Suri, [Ionics](#) **16**, 833 (2010).